International Journal of Science and Research (IJSR)
ISSN: 2319-7064
Impact Factor 2024: 7.101

Numerical Simulation of Seismic Wave Propagation in Attenuative and Heterogeneous Media

Bernard Adero

National Defence University-Kenya, P.O BOX 3812 - 20100, Nakuru, Kenya
Corresponding Author Email: *botieno[at]ndu.ac.ke*

Abstract: ***In this study, we present a forward numerical simulation approach to investigate seismic wave propagation in attenuative and heterogeneous geological media. Using a finite difference method to solve two-dimensional viscoelastic wave equations, the research evaluates the effects of attenuation on wave amplitude and dispersion. By comparing lossy and non-lossy models, the study highlights how attenuation alters seismic waveforms and how compensation techniques can restore energy loss. Numerical tests in both homogeneous and heterogeneous media, including a modified Barnett Shale model, demonstrate the model's ability to replicate realistic seismic scenarios. This suggests that the proposed approach is a valuable tool for improving seismic interpretation, particularly in contexts where wave attenuation complicates imaging processes.***

Keywords: seismic wave simulation, viscoelastic media, attenuation modeling, anisotropic propagation, finite difference method

1. Introduction

The propagation of seismic waves through geological structures represents a pivotal area of investigation in the comprehension and mitigation of seismic activity (Kerato et al., 2008; Russo & Silver, 1994). Seismic wave propagation correlates with geophysical structures (Virieux & Operto, 2009; Zhu et al., 2020). Analyzing stress-wave propagation is crucial in understanding mechanical properties (Brossier et al., 2009; Tromp, 2020). One of the most prevalent methodologies in the field of seismic-wave studies is the inversion of seismic waves (Harris et al, 2018; Pageot et al., 2013). This technique functions in a manner analogous to a geophysical X-ray, utilizing data derived from the Earth's surface to construct a comprehensive image of the underlying geological structures (Chi et al., 2014; Zhu et al., 2020). Seismic-wave inversion has become a standard practice in the oil and gas industry for mapping the subterranean terrain, due to its high degree of accuracy (Harris et al., 2018; Zhang & Toksöz 1998; Taillandier et al., 2009).

In the field of seismic-wave inversion, numerical simulations have become an indispensable tool for advancing scientific understanding (Almuhaidib &Toksoez (2015); Kristeková et al., (2009); Shragge & Konuk (2020)). Seismic wave simulations offer valuable insights into earthquake-induced activity, helping quantify potential surface disruptions (Zang et al., 2021). The incorporation of parameters that accurately reflect the characteristics of the medium of the Earth into seismic-wave simulations has the potential to enhance our theoretical understanding of these phenomena Zang et al., (2021). These simulations are not just tools; they provide insight into the propagation of seismic waves, thereby improving the accuracy of seismic-wave inversion techniques Etienne (2010).

One of the fundamental properties of wave propagation is the conversion of elastic energy into heat. Anelastic effects, quantified by the quality factor Q, can lead to amplitude reduction and wavelet distortion. As an example, the presence of low saturation gas in sediments can cause strong attenuation of seismic P-waves. The attenuation effects result in a dimming of migrated amplitudes below the gas. Since the high-frequency components of seismic data are more strongly attenuated than the low-frequency ones, the effects also reduce resolution in the image. Consequently attenuation compensation is necessary to improve structural imaging and interpretation.

Given a Q model, a viscoelastic mechanical model consisting of standard linear solids (SLSs) provides a powerful tool to model real earth materials (Robertsson et al., 1994). One SLS consists of a spring in parallel with a spring and a dashpot in series. It can approximate a constant Q within a defined frequency band. A series of SLSs connected in parallel can yield a quite general mechanical viscoelasticity (Day and Minster, 1984). In an SLS the stress-strain relationship is expressed as a causal time convolution of a stress relaxation function with the strain rate (Liu et al., 1976; Day and Minster, 1984; Carcione, 2001; Robertsson et al., 1994). This time dependence of the relaxation mechanism is governed by the stress and strain relaxation times. They describe the physical dissipation mechanism that the real earth materials have on wave propagation. Finite-difference wavefield extrapolations implemented on staggered grids have shown that the SLSs can simulate wave propagation well (Robertsson et al., 1994). Carcione (1999) derived the time-domain viscoelastic equation for wave propagation in a heterogeneous VTI medium. Wave equation for forward modeling and its adjoint, is solved by finite-different methods on centered grids to estimate velocity and Q models in viscoelastic waveform. In the equations memory variables simulate viscosity.

The anisotropic forward modeling is based on lossy and non-lossy elastic VTI wave equations derived from first principles, without any other approximation than the acoustic VTI approximation itself. This approach leads to a set of first order differential equations in the components of the particle velocity vector and two independent stress components and has a number of clear advantages: All involved variables have a clear physical meaning, the variable density case is handled in a natural way, and C-PML absorbing boundaries are easily incorporated.

Paper ID: SR25716160251 DOI: https://dx.doi.org/10.21275/SR25716160251

The primary purpose of this research is to develop and validate a numerical simulation model for analyzing seismic wave propagation in attenuative and anisotropic heterogeneous media using finite difference methods.

This study is significant because it provides computational tools for more accurate seismic imaging in complex geological settings, aiding applications in earthquake analysis, oil and gas exploration, and subsurface mapping.

2. Equations for simulating the propagation of seismic waves

2.1 Elastic wave equation in VTI anisotropic medium

We examine wave propagation in a two-dimensional medium in this paper. The stress-strain relation is derived from the constitutive relations of the transversely isotropic medium, where x and z stand for the horizontal and vertical components, respectively (Carcione, 1988) and it is written as,

$$\begin{bmatrix}\sigma_{xx}\\ \sigma_{zz}\\ \sigma_{xz}\end{bmatrix}=\begin{bmatrix}c_{11} & c_{13} & 0\\ c_{13} & c_{33} & 0\\ 0 & 0 & c_{44}\end{bmatrix}\begin{bmatrix}\varepsilon_{xx}\\ \varepsilon_{zz}\\ 2\varepsilon_{xz}\end{bmatrix} \tag{1.1}$$

where σ_{ij} and ε_{ij} are stress and strain components of the medium, and c_{ij} are the elasticities of the medium.

The constitutive relation and momentum conservation are used to describe the propagation of waves (Carcione, 1988). For a continuous medium, the linearized equation of motion is provided by

$$\rho\frac{\partial^2 u}{\partial t^2}=\nabla.\Sigma+f \tag{1.2}$$

Where $u(x,t)$ is the displacement field, $\Sigma(x,t)$ is the stress tensor, $f(x,t)$ represents the body forces, and $\rho(x)$ is the density. For two-dimensional solid, equation (1.2) is written as:

$$\rho\frac{\partial^2 u_x}{\partial t^2}=\frac{\partial\sigma_{xx}}{\partial x}+\frac{\partial\sigma_{xz}}{\partial z}+f_x \tag{1.3}$$

$$\rho\frac{\partial^2 u_z}{\partial t^2}=\frac{\partial\sigma_{zx}}{\partial x}+\frac{\partial\sigma_{zz}}{\partial z}+f_z \tag{1.4}$$

where the components of displacements and body forces are denoted by u_x and u_z and f_x and f_z respectively. Using the strain-displacement relation and replacing the constitutive relation in equations of motion (1.3-1.4), we obtain,

$$\rho\frac{\partial^2 u_x}{\partial t^2}=\frac{\partial}{\partial x}\left[c_{11}\frac{\partial u_x}{\partial x}+c_{13}\frac{\partial u_z}{\partial z}\right]+\frac{\partial}{\partial z}\left[c_{44}\left(\frac{\partial u_x}{\partial z}+\frac{\partial u_z}{\partial x}\right)\right]+f_x \tag{1.5}$$

$$\rho\frac{\partial^2 u_z}{\partial t^2}=\frac{\partial}{\partial z}\left[c_{13}\frac{\partial u_x}{\partial x}+c_{33}\frac{\partial u_z}{\partial z}\right]+\frac{\partial}{\partial x}\left[c_{44}\left(\frac{\partial u_x}{\partial z}+\frac{\partial u_z}{\partial x}\right)\right]+f_z \tag{1.6}$$

Equations (1.5-1.6) are a particular example of the equations of motion for vertical transverse isotropic (VTI) media. It follows that,

$$c_{11}=c_{33}(2\varepsilon+1) \tag{1.7}$$

$$c_{33}=\alpha^2\rho \tag{1.8}$$

$$c_{44}=\beta^2\rho \tag{1.9}$$

$$c_{13}=\sqrt{(c_{33}-c_{44})^2+2\delta c_{33}(c_{33}-c_{44})}+c_{44} \tag{1.10}$$

2.2 Viscoelastic wave equation in VTI anisotropic medium

Carcione (1999) derives the time-domain viscoelastic equation for wave propagation in a heterogeneous VTI medium. The following constitutive equations provide a complete description of the two-dimensional velocity-stress formulation for anelastic propagation in the (x,z)-plane, where one relaxation mechanism is attributed to dilational anelastic deformations (ν=p) and another to shear anelastic deformations (ν=s):

$$\frac{\partial\sigma_{xx}}{\partial t}=c_{11}\frac{\partial v_x}{\partial x}+c_{13}\frac{\partial v_z}{\partial z}+K^0e_1+2c_{44}^0e_2 \tag{1.11}$$

$$\frac{\partial\sigma_{zz}}{\partial t}=c_{13}\frac{\partial v_x}{\partial x}+c_{33}\frac{\partial v_z}{\partial z}+K^0e_1-2c_{44}^0e_2 \tag{1.12}$$

$$\frac{\partial\sigma_{xz}}{\partial t}=c_{44}\left(\frac{\partial v_x}{\partial x}+\frac{\partial v_z}{\partial z}\right)+2c_{44}^0e_3 \tag{1.13}$$

where e_1, e_2 and e_3 are memory variables, while c_{11}, c_{13}, c_{33} and c_{44} are unrelaxed stiffness coefficients, v_x and v_z are the particle velocities; σ_{ij} are the stress components.

$$\text{The value } K^0=\frac{1}{2}\left(c_{11}^0+c_{33}^0\right)-c_{44}^0 \tag{1.14}$$

The relaxed stiffness coefficients are

$$c_{11}^0=c_{11}-D+K\tau_p+c_{44}\tau_s \tag{1.15}$$

$$c_{33}^0=c_{33}-D+K\tau_p+c_{44}\tau_s \tag{1.16}$$

$$c_{13}^0=c_{13}-D+K\tau_p+c_{44}(2-\tau_s) \tag{1.17}$$

$$c_{44}^0=c_{44}\tau_s \tag{1.18}$$

with

$$K=D-c_{44} \tag{1.19}$$

$$D=\frac{1}{2}(c_{11}+c_{33}) \tag{1.20}$$

and

Paper ID: SR25716160251 DOI: https://dx.doi.org/10.21275/SR25716160251

$$\tau_v = \frac{\tau_\sigma^{(v)}}{\tau_\varepsilon^{(v)}} \qquad (1.21)$$

The material relaxation times, represented by the values τ_σ and τ_ε correspond to shear and dilational deformations, respectively. The equations for the memory variable are

$$\frac{\partial e_1}{\partial t} = \frac{1}{\tau_\sigma^p}\left[(1-\frac{1}{\tau_p})(\frac{\partial v_x}{\partial x}+\frac{\partial v_z}{\partial z}) - e_1\right] \qquad (1.22)$$

$$\frac{\partial e_2}{\partial t} = \frac{1}{2\tau_\sigma^s}\left[(1-\frac{1}{\tau_s})(\frac{\partial v_x}{\partial x}-\frac{\partial v_z}{\partial z}) - 2e_2\right] \qquad (1.23)$$

$$\frac{\partial e_3}{\partial t} = \frac{1}{\tau_\sigma^s}\left[(1-\frac{1}{\tau_s})(\frac{\partial v_x}{\partial z}+\frac{\partial v_z}{\partial x}) - e_3\right] \qquad (1.24)$$

3. Methods

3.1 Finite difference scheme

For the finite-difference model, a velocity-stress formulation of the first order is selected. The discretization of the stress-strain relation and the equations of motion for a viscoelastic wave, found in Equations (1.11–1.13), results in a set of first-order partial differential equations. The three unknown stress components σxx, σxz, σzz, as well as the two unknown particle velocities v_x and v_z, are the only non-zero field components because only field components in the x-z plane are stimulated. A set of five partial differential equations thus fully describes the motion of the waves:

$$\frac{\partial v_x}{\partial t} = \frac{\partial \sigma_{xx}}{\partial x} + \frac{\partial \sigma_{xz}}{\partial z} \qquad (1.25)$$

$$\frac{\partial v_z}{\partial t} = \frac{\partial \sigma_{xz}}{\partial x} + \frac{\partial \sigma_{zz}}{\partial z} \qquad (1.26)$$

$$\frac{\partial \sigma_{xx}}{\partial t} = c_{11}\frac{\partial v_x}{\partial x} + c_{13}\frac{\partial v_z}{\partial z} + K^0 e_1 + 2c_{44}^0 e_2 \qquad (1.27)$$

$$\frac{\partial \sigma_{zz}}{\partial t} = c_{13}\frac{\partial v_x}{\partial x} + c_{33}\frac{\partial v_z}{\partial z} + K^0 e_1 - 2c_{44}^0 e_2 \qquad (1.28)$$

$$\frac{\partial \sigma_{xz}}{\partial t} = c_{44}(\frac{\partial v_x}{\partial x} + \frac{\partial v_z}{\partial z}) + 2c_{44}^0 e_3 \qquad (1.29)$$

For instance, Equations (1.25) and (1.27), which introduce the finite differences in space (Δx and Δz) and time (Δt), can be discretized as

$$\frac{V_x^{k+0.5}(i-0.5,j-0.5)-V_x^{k-0.5}(i-0.5,j-0.5)}{\Delta t} = \frac{\sigma_{xx}^k(i,j-0.5)-\sigma_{xx}^k(i-1,j-0.5)}{\Delta x} + \frac{\sigma_{xz}^k(i-0.5,j)-\sigma_{xz}^k(i-0.5,j-1)}{\Delta z} \qquad (1.30)$$

$$\frac{\sigma_{xx}^{k+1}(i,j-0.5)-\sigma_{xx}^k(i,j-0.5)}{\Delta t} = c_{11}\frac{V_x^{k+0.5}(i+0.5,j-0.5)-V_x^{k+0.5}(i-0.5,j-0.5)}{\Delta x} + c_{13}\frac{V_z^{k+0.5}(i,j)-V_z^{k+0.5}(i,j-1)}{\Delta z} + K^0 e_1 + 2c_{44}^0 e_2 \qquad (1.31)$$

Here, the numerical values of the correspondent field component at a specific point in time and space are denoted by V_i and σ_{ij}.

$V_x^{k+0.5}(i-0.5,j-0.5)$ represents, for instance, the numerical value of the particle velocity v_x at $(x,z)=((i-0.5)\Delta x,(j-0.5)\Delta z)$ and time $t=(k+0.5)\Delta t$. Knowing $V_x^{k-0.5},\sigma_{xx}^k,\sigma_{xz}^k$, Equation (1.30) can be solved for $V_x^{k+0.5}$, that is, at the increment time $t=(k+0.5)\Delta t$:

$$V_x^{k+0.5}(i-0.5,j-0.5) = V_x^{k-0.5}(i-0.5,j-0.5) + \frac{\Delta t}{\Delta x}(\sigma_{xx}^k(i,j-0.5)-\sigma_{xx}^k(i-1,j-0.5)) + \frac{\Delta t}{\Delta z}(\sigma_{xz}^k(i-0.5,j)-\sigma_{xz}^k(i-0.5,j-1)) \qquad (1.32)$$

Similarly, σ_{xx}^{k+1} is obtained from Equation (1.31):

$$\sigma_{xx}^{k+1}(i,j-0.5) = \sigma_{xx}^k(i,j-0.5) + c_{11}\frac{\Delta t}{\Delta x}(V_x^{k+0.5}(i+0.5,j-0.5)-V_x^{k+0.5}(i-0.5,j-0.5)) + c_{13}\frac{\Delta t}{\Delta z}(V_z^{k+0.5}(i,j)-V_z^{k+0.5}(i,j-1)) + \Delta t(K^0 e_1 + 2c_{44}^0 e_2) \qquad (1.33)$$

Discrete equations for each of the field components can be generated in the same way. It is crucial to stress that the velocity and stress components are offset by Δt/2 in time and by Δx/2 and Δz/2 in space, and are not known at the same location in both space and time. As a result, the leapfrog algorithm and staggered grid are introduced. The field components in this technique are updated in time in a sequential manner. In other words, the velocity components are computed first, followed by the stress components, the velocity components again using the stress components, and so on. Therefore, the field components for all subsequent times $t>t_0$ may be found by knowing the field components across the entire space at times t_0 and $t_0 + 0.5\Delta t$, respectively.

4. Result and discussion

4.1 Forward simulations

4.1.1 Homogeneous medium

In Figure 1.3 (a-d), we show the snapshots of horizontal component wave fields of viscoelastic wave propagation at time, t = 0.6 s, in a homogeneous medium with different quality factors, $\varepsilon = 0.24$, $\delta = 0.1$. The grid spacing for the 4000 m by 4000 m model is $\Delta x = \Delta z = 10$ m. Density 3.0 g/cm3, S-wave velocity vs = 1930 m/s, and P-wave velocity vp = 2500 m/s. 15 Hz is used as the reference frequency to define the phase velocities. A Ricker wavelet with a dominating frequency of 25 Hz is excited by an explosive source positioned in the middle of the model.

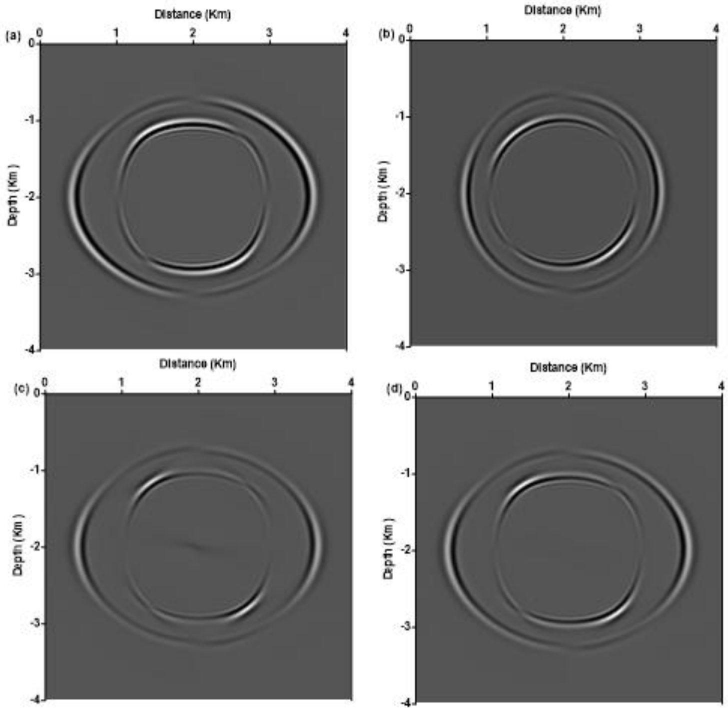

Figure 1.3: Wavefield snapshots at 600 ms in a homogeneous medium including (a) elastic VTI; (b) attenuative isotropic medium with Qp = Qs = 40; (c) attenuative VTI medium with Qp = Qs = 40 and $\varepsilon = 0.24$, $\delta = 0.1$; and (d) attenuative VTI medium with Qp = Qs = 100, $\varepsilon = 0.24$, $\delta = 0.1$.

With attenuation Q-factors of Qp = 100 and Qs = 80 for P-wave and S-wave attenuations, respectively, a receiver positioned at (3000 m, 1500 m) in the simulation model captures the waveform for anisotropic viscoelastic wave propagation without attenuation compensation (viscoelastic vti) and for anisotropic viscoelastic wave propagation with attenuation compensation (viscoelastic_TR). These recorded waveforms are compared to the recorded waveform of the reference anisotropic elastic wave propagation in the same model. In Figure 1.4, it can be seen that the amplitude of the waveform received for anisotropic viscoelastic wave propagation (viscoelastic vti) is more attenuated compared to the reference anisotropic elastic wave propagation, which has zero attenuation. The amplitude of S-wave in the viscoelastic vti waveform is more attenuated than the amplitude of P-wave of the same waveform. This is because of the attenuation Q-factor of S-wave which has higher attenuation value than that of P-wave.

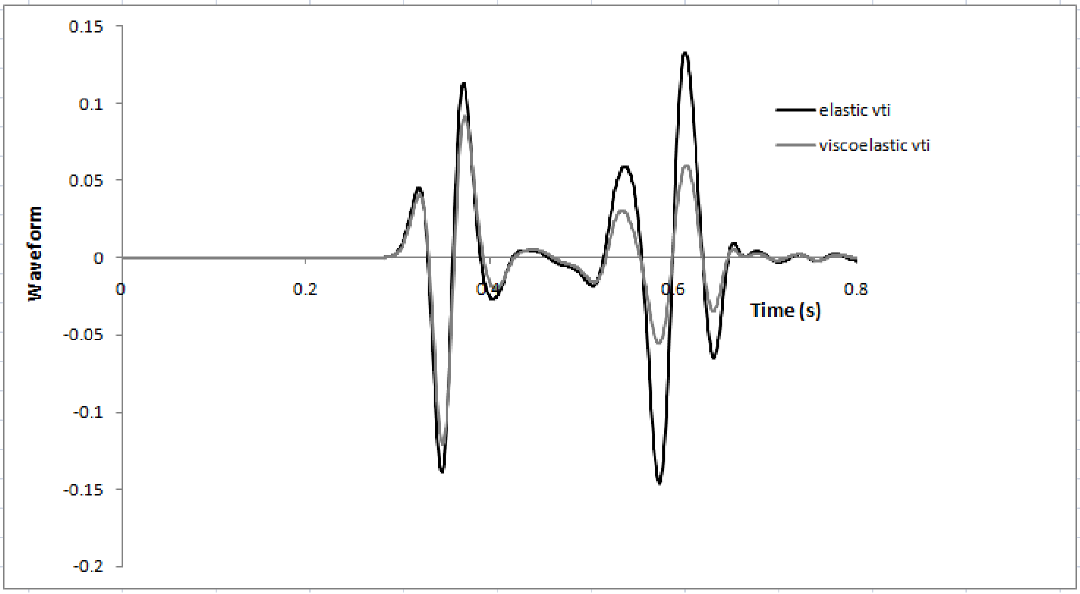

Figure 1.4: Comparison of anisotropic elastic waveform (black line) and anisotropic viscoelastic waveform (grey line).

Anisotropic viscoelastic wave propagation with attenuation compensation corrects for the loss of energy during propagation (Fig. 1.5). The waveform recorded by the same receiver in the model show the amplitude closely matches that of the reference anisotropic elastic wave propagation, with zero attenuation.

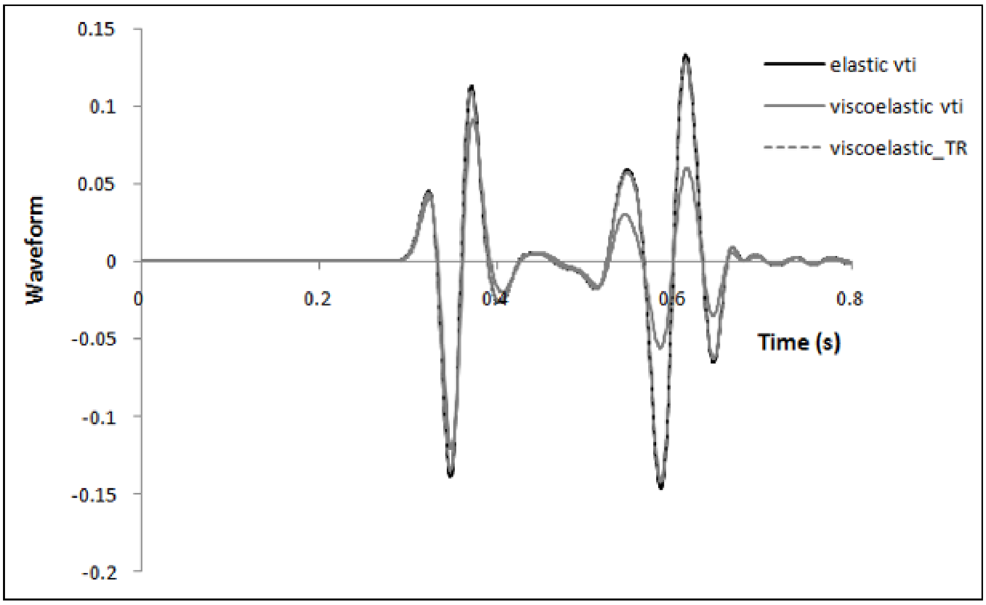

Figure 1.5: Comparison of anisotropic elastic waveform (black line), anisotropic viscoelastic waveform (grey line) and anisotropic viscoelastic waveform with attenuation compensation (broken grey line).

4.1.2 Heterogeneous medium

With a low velocity shale layer surrounded by high velocity strata, we create a synthetic seismogram using a modified Barnet Shale model (Maxwell, 2009) (Fig. 1.6). There are 400 x 400 gridpoints in the discretized model. A time-varying Ricker wavelet with a peak frequency of 100 Hz is injected as a point source, beginning with a single source situated at (200 m, 200 m). With the horizontal and vertical axes grid spaced as follows: $\Delta x = \Delta z = 1.0$ m, a time step of 0.1 ms is employed. 36 receivers are placed 10 meters apart at depths between 50 and 400 meters. In Figure 1.6, the source-receiver geometry is displayed. A forward modeling anisotropic viscoelastic code employing finite differences produced synthetic data. Figures 1.7 and 1.8, respectively, display the horizontal stress components that resulted from the reference anisotropic elastic and anisotropic viscoelastic seismograms.

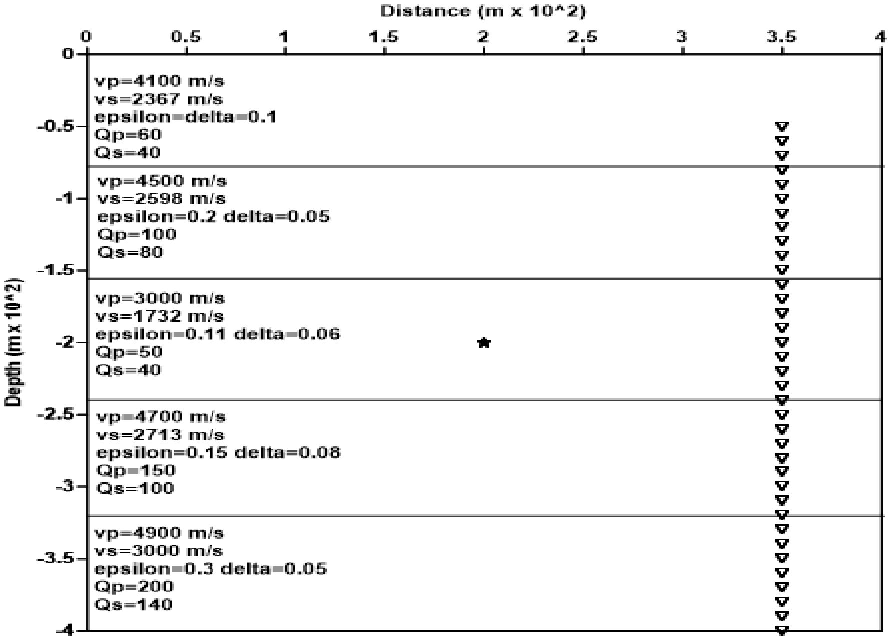

Figure 1.6: Source-receiver geometry on modified Barnet Shale velocity model.

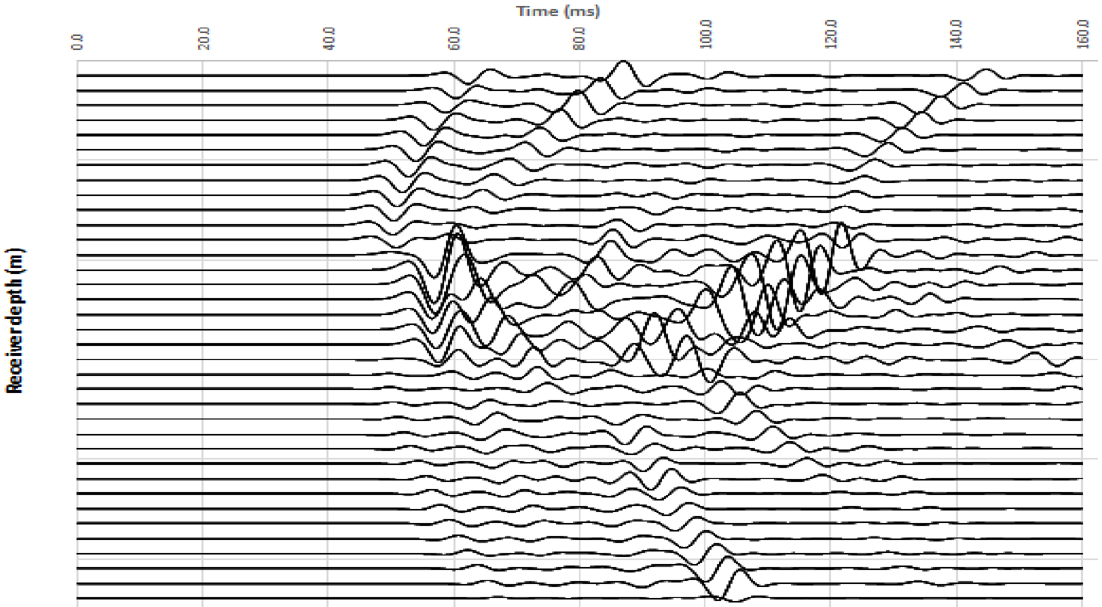

Figure 1.7: Seismograms recorded at the receiver array, as determined by an elastic (anisotropic) solver.

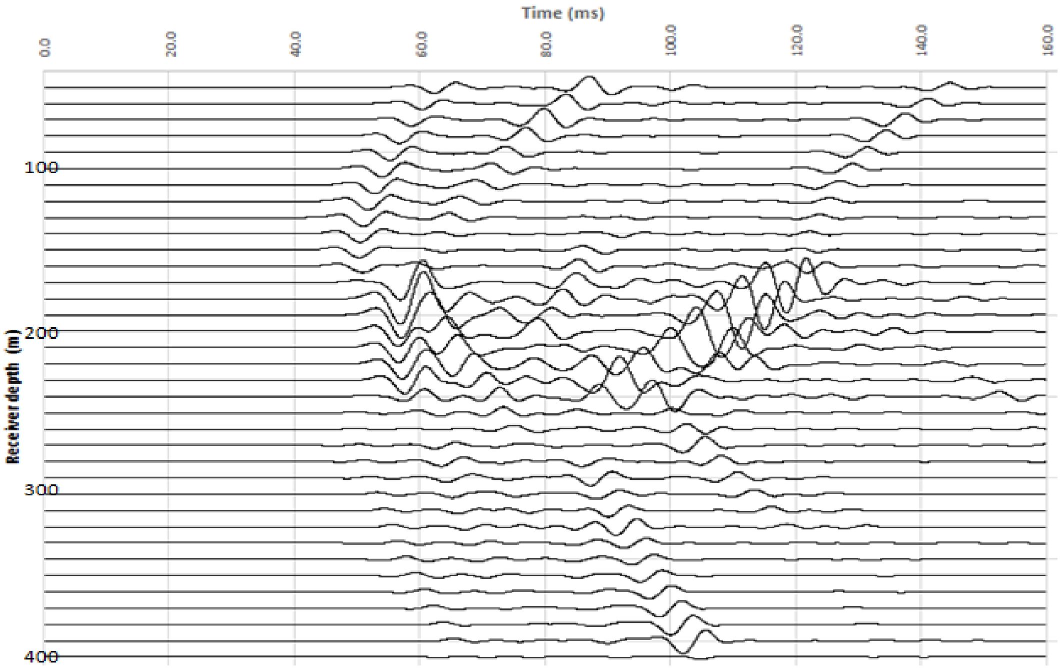

Figure 1.8: Seismograms recorded at the receiver array, as determined by an anisotropic viscoelastic solver.

One benefit of the time reversal approach is its ability to tolerate noise. Numerical simulations of anisotropic viscoelastic media are possible. Figure 1.9 illustrates the addition of Gaussian random noise to the original signal following the vertical array's recording of the signal from the source (Fig. 1.8).

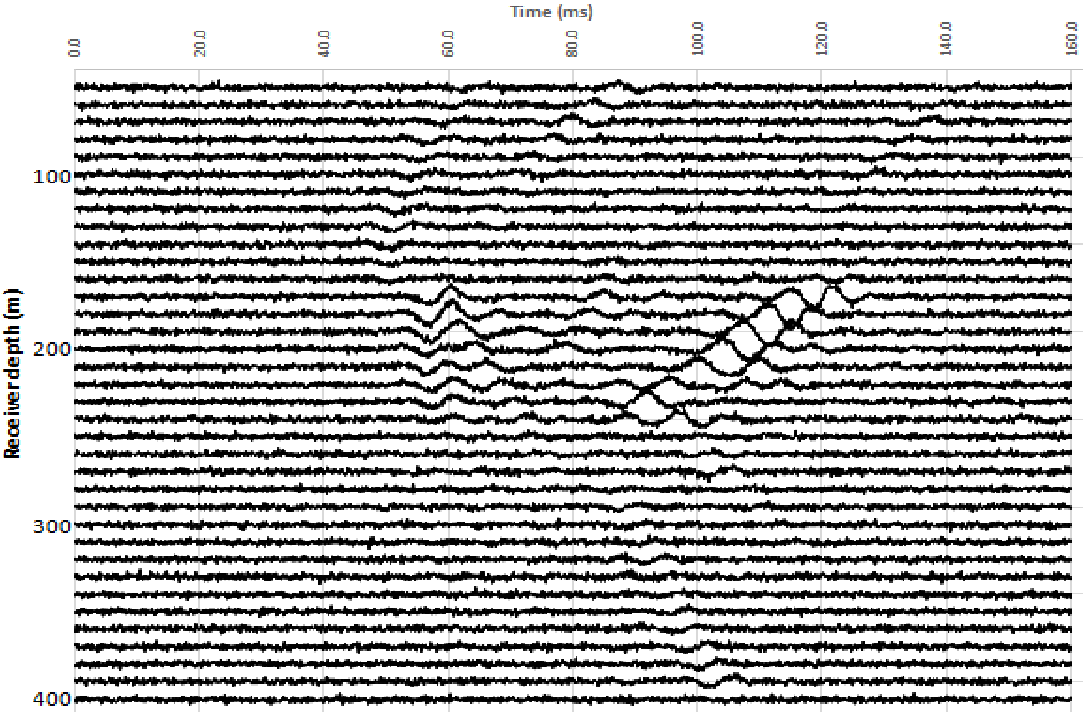

Figure 1.9: Recorded seismogram contaminated with Gaussian noise.

5. Conclusion

This research demonstrates that attenuation significantly alters both the amplitude and phase of seismic waveforms in heterogeneous and anisotropic media. The use of numerical simulation techniques, particularly those compensating for attenuation, proves effective in restoring wave energy profiles to those of non-attenuative models. In my view, this suggests a promising pathway for improving subsurface imaging in geophysics, where accurate representation of wave behavior is crucial for interpretation and decision-making.

References

[1] Almuhaidib, A.M.; Toksoez, M.N. Finite difference elastic wave modeling with an irregular free surface using ADER scheme. J. Geophys. Eng. 2015, 12, 435–447.

[2] Bai, J., D. Yingst, R. Bloor, and J. Leveille, 2012, Waveform inversion with attenuation: 82nd Annual International Meeting, SEG Expanded Abstracts.

[3] Bai, J., D. Yingst, G. Chen, and J. Leveille, 2013, Attenuation compensation in viscoacoustic reverse time

migration: 83rd Annual International Meeting, SEG Expanded Abstracts.

[4] Blanch, J. O., and W. W. Symes, 1995, Efficient iterative viscoacoustic linearized inversion: 65th Annual International Meeting, SEG, Expanded Abstracts, 627–630.

[5] Brossier, R.; Operto, S.; Virieux, J. Seismic imaging of complex onshore structures by 2D elastic frequency-domain full-waveform inversion. Geophysics 2009, 74, WCC105–WCC118.

[6] Carcione, J. M. 2001 *Wave Fields in Real Media: Wave Propagation in Anisotropic, Anelastic and Porous Media* (New York: Pergamon).

[7] Carcione, J.M. 1999, Staggered mesh for the anisotropic and viscoelastic wave equation: Geophysics, 64(6), 1863-1866.

[8] Carcione, J. M., Kosloff, D., and Kosloff, R., 1988, Viscoacoustic wave propagation simulation in the earth: Geophysics, **53**(6), 769 – 777.

[9] Chi, B.; Dong, L.; Liu, Y. Full waveform inversion method using envelope objective function without low frequency data. J. Appl. Geophys. 2014, 109, 36–46.

[10] Day, S. M., and J. B. Minster, 1984, Numerical simulation of wave fields using a Padé approximant method: Geophysical Journal of the Royal Astronomical Society, 78, no. 1, 105–118, http://dx.doi.org/10.1111/j.1365-246X.1984.tb06474.x.

[11] Duveneck E and Bakker P M 2011 Stable P-wave modeling for reverse time migration in tilted TI media *Geophysics* **76** S65–75.

[12] Duveneck, E., Milcik, P., Bakker, P.M. & Perkins, C., 2008. Acoustic VTI wave equations and their application for anisotropic reverse-time migration, in Proceedings of 78th Ann. Int. Meeting, SEG, Expanded Abstracts, pp. 2186–2190.

[13] El Sahmarany, L., L. Berry, K. Kerroum, F. Auzanneau, and P. Bonnet, 2012, Time reversal for wiring diagnosis, Electronics Letters, Vol. 48, No. 21, 1343-1344.

[14] Erwemi, A., Walsh, J., Bennett, L., Woerpel, C., and Purcel, D., 2010, Anisotropic velocity modeling for microseismic processing: Part3-borehole sonic calibration: SEG Denver annual meeting, 508-512.

[15] Etienne, V.; Chaljub, E.; Virieux, J.; Glinsky, N. An hp-adaptive discontinuous Galerkin finite-element method for 3-D elastic wave modelling. Geophys. J. Int. 2010, 183, 941–962.

[16] Fink, M., 2006, Time-reversal acoustics in complex environments: Geophysics, 71, no. 4, SI151– SI164.

[17] Gandossi, L., 2013, An overview of hydraulic fracturing and other formation stimulation technologies for shale gas production: Scientific and Technical Research series (Report).

[18] Gosselet, A., and S. C. Singh, 2007, Using symmetry breaking in time reversal mirror for attenuation determination: 77th Annual International Meeting, SEG, Expanded Abstracts, 1639–1643.

[19] Gajewski, D. and Tessmer, E. [2005] Reverse modelling for seismic event characterization. *Geophys. J. Int*, 163,276–284.

[20] Harris, C.W.; Miller, M.S.; Porritt, R.W. Tomographic Imaging of Slab Segmentation and Deformation in the Greater Antilles. Geochem. Geophys. Geosyst. 2018, 19, 2292–2307.

[21] Hustedt, B., S. Operto, and J. Virieux, 2004, Mixed-grid and staggered-grid finite difference methods for frequency domain acoustic wave modelling: Geophysical Journal International, **157**, 1269–1296.

[22] Kao, H. & Shan, S. J., 2004. The source-scanning algorithm: mapping the distribution of seismic sources in time and space, *Geophys. J. Int.,* **157,**589–594.

[23] Karato, S.-I.; Jung, H.; Katayama, I.; Skemer, P. Geodynamic significance of seismic anisotropy of the upper mantle: New insights from laboratory studies. Annu. Rev. Earth Planet. Sci. 2008, 36, 59–95.

[24] Kawakatsu, H., and J. P. Montagner, 2008, Time-reversal seismic-source imaging and Moment-tensor inversion: Geophysical Journal International, 175, 686–688.

[25] Kremers, S., A. Fichtner, G. Brietzke, H. Igel, C. Larmat, L. Huang, and M.Käser, 2011, Exploring the potentials and limitations of the time-reversal imaging of finite seismic sources: Solid Earth, 2, 95–105.

[26] Kristeková, M.; Kristek, J.; Moczo, P. Time-frequency misfit and goodness-of-fit criteria for quantitative comparison of time signals. Geophys. J. Int. 2009, 178, 813–825.

[27] Larmat, C.S., Guyer, R.A. & Johnson, P.A., 2009. Tremor source location using time reversal: Selecting the appropriate imaging field, *Geophys. Res.Lett.,* **36,** L22304.

[28] Liu, H.-P., D. L. Anderson, and H. Kanamori, 1976, Velocity dispersion due to anelasticity; implications for seismology and mantle composition: Geophysical Journal of the Royal Astronomical Society, 47, no. 1, 41–58, http://dx.doi.org/10.1111/j.1365-246X.1976.tb01261.x

[29] Lomax, A., Virieux, J., Voulant, P. and Berge-Thierry, C. 2000. Introduction of a metropolis-gibbs method and comparison with linear locations. Klumer Academic Publisher, chap: Probabilistic earthquake location in 3D and layered models, 101-134.

[30] Lu, R., 2007. Time reversed acoustics and applications to earthquake location and salt dome flank imaging, *PhD thesis*, Massachusetts Institute of Technology.

[31] Lu, R., Toks¨oz, M.N. & Willis, M.E., 2008. Locating microseismic events with time reversed acoustics: a synthetic case study, in *Proceedings of the78th Annual International Meeting, SEG,* Expanded Abstracts, pp. 1342–1346.

[32] Maxwell, S., 2009, Microseismic location uncertainty: CSEG Recorder, 41-46.

[33] McMechan, G.A., 1982. Determination of source parameters by wavefield extrapolation, *Geophys. J. R. astr. Soc.,* **71,** 613–628.

[34] McMechan, G.A., Luetgert, J.H. and Mooney, W.D. [1985] Imaging of earthquake sources in long valley caldera, California, 1983. *Bull. seism. Soc. Am.*, 75(4), 1005–1020.

[35] Norville, P. D., W. R. Scott, Jr., and G. D. Larson, 2004, an investigation of time reversal techniques in seismic landmine detection: Proceedings of SPIE, 5415, 1310–1322.

[36] O'Brien, G., Lokmer, I., Barros, L.D., Bean, C., Saccorotti, G., Metaxian,J. P. & Patane, D., 2011. Time reverse location of seismic long-period events recorded on Mt. Etna, *Geophys. J. Int.,* **184,** 452–462.

[37] Operto, S., A. Ribodetti, M. Grini, and J. Virieux, 2009, Finite difference frequency-domain viscoacoustic wave modeling in 2D TTI anisotropic media: Geophysics, 74(5), 75-95.

[38] Pageot, D.; Operto, S.; Vallée, M.; Brossier, R.; Virieux, J. A parametric analysis of two-dimensional elastic full waveform inversion of teleseismic data for lithospheric imaging. Geophys. J. Int. 2013, 193, 1479–1505.

[39] Robertsson, J. O. A., J. O. Blanch, and W. W. Symes, 1994, Viscoelastic finite-difference modeling: Geophysics, **59**, 1444–1456.

[40] Russo, R.M.; Silver, P.G. Trench-parallel flow beneath the nazca plate from seismic anisotropy. Science 1994, 263, 1105–1111.

[41] Saenger, E. H., 2011, Time reverse characterization of sources in heterogeneous media: Independent Nondestructive Testing and Evaluation International, 44, 751–759.

[42] Shragge, J.; Konuk, T. Tensorial elastodynamics for isotropic media. Geophysics 2020, 85, T359–T373.

[43] Snieder, R., 2007, Extracting the Green's function of attenuating acoustic media from uncorrelated waves: Journal of the Acoustical Society of America, 121, 2637–2643.

[44] Steiner, B., E. H. Saenger, and S. M. Schmalholz, 2008, Time reverse modelling of microtremors: Application to hydrocarbon reservoir localization: Geophysical Research Letters, 35, L03307.

[45] Taillandier, C.; Noble, M.; Chauris, H.; Calandra, H. First-arrival traveltime tomography based on the adjoint-state method. Geophysics 2009, 74, WCB1–WCB10.

[46] Thorbecke, J. W., and D. Draganov, 2011, Finite-difference modeling experiments for seismic interferometry: Geophysics, **76**, no. 6, H1–H18.

[47] Tromp, J. Seismic wavefield imaging of Earth's interior across scales. Nat. Rev. Earth Environ. 2020, 1, 40–53.

[48] Verdon, J.P., Kendall, J.M., White, D.J., Angus, D.A., Fisher, Q.J., and Urbancic, T. 2010, Passive seismic monitoring of carbon dioxide storage at Weyborn. The Leading Edge, 29, 200-206.

[49] Virieux, J.; Operto, S. An overview of full-waveform inversion in exploration geophysics. Geophysics 2009, 74, WCC1–WCC26.

[50] Waldhauser, F. and Ellsworth, W.L. 2001, A double difference earthquake location algorithm: Method and application to the northern Hayward fault, California. Bull. Seism. Soc. Am., 90, 1355-1368.

[51] Warpinski, N., Waltman, C.K., Du, J., and Ma, Q., 2009, Anisotropy effects in microseismic monitoring, SPE124208.

[52] Wencai, X., Zhenchun, L., Wenshi, D., and Jiao, W., 2015, Anisotropic viscoacoustic wave RTM based on second-order quasi-differential equation: 85th Annual International Meeting, SEG Expanded Abstracts.

[53] Zang, N.; Zhang, W.; Chen, X. An overset-grid finite-difference algorithm for simulating elastic wave propagation in media with complex free-surface topography. Geophysics 2021, 86, T277–T292.

[54] Zhang, J.; Toksöz, M.N. Nonlinear refraction traveltime tomography. Geophysics 1998, 63, 1726–1737.

[55] Zhu, T., 2014, Time reverse modeling of acoustic wave propagation in attenuating media: Geophysical Journal International, 197, 483–494.

[56] Zhu, T., 2015, Viscoelastic time reversal imaging: Geophysics, vol. 8, No. 2, 1–6.

[57] Zhu, H.; Stern, R.J.; Yang, J. Seismic evidence for subduction-induced mantle flows underneath Middle America. Nat. Commun. 2020, 11, 2075.

[58] Zhu, H.; Yang, J.; Li, X. Azimuthal Anisotropy of the North American Upper Mantle Based on Full Waveform Inversion. J. Geophys. Res. Solid Earth 2020, 125, 18432.